Compressible sponge electrodes by oxidative molecular layer deposition (oMLD) of polyethylenedioxythiophene (PEDOT) onto open-cell polyurethane sponges

Mahya Mehregan,¹ David Stalla,² Gabe Luebbert,³ Lauren Baratta,³ Katrina G. Brathwaite,³ Quinton K. Wyatt,¹ Nikhila C. Paranamana,¹ Matthias J. Young,^{1,3,4*}

³Department of Chemical and Biomedical Engineering, University of Missouri, Columbia, MO, USA

I. Abstract:

The formation of compressible porous sponge electrodes is appealing to overcome diffusion limitations in porous electrodes for applications including electrochemical energy storage, electrochemical water desalination, and electrocatalysis. Previous work has employed wet chemical synthesis to deliver conductive materials into porous polymer sponge supports, but these approaches struggle to produce functional electrodes due to (1) poor electrical connectivity of the conductive network and (2) mechanical rigidity of the foam after coating. In this work we employ oxidative molecular layer deposition (oMLD) via sequential gas-phase exposures of 3,4 ethylenedioxythiophene (EDOT) and molybdenum pentachloride (MoCl₅) oxidant to imbibe with electrically-conductive polyurethane sponges and redox-active poly(3,4)ethylenedioxythiophene) (PEDOT) coatings. We analyze the oMLD deposition on compressive polyurethane sponges and modify the reaction conditions to obtain mechanically compressible and electrically conductive sponge electrodes. We specifically identify the importance MoCl₅ dose time to enhance the conductivity of the sponges and the importance of EDOT purge time to preserve the mechanical properties of the sponges. Controlling these variables produces an electrically conductive PEDOT network within the sponge support with reduced impact on the sponge's mechanical properties, offering advantages over wet-chemical synthesis approaches. The compressible, conductive sponges we generate have the potential to be used as compressible electrodes for water desalination, energy storage, and electrocatalysis.

¹Department of Chemistry, University of Missouri, Columbia, MO, USA

²Electron Microscopy Core, University of Missouri, Columbia, MO, USA

⁴Materials Science and Engineering Institute, University of Missouri, Columbia, MO, USA

^{*}Email: matthias.young@missouri.edu

II. Introduction:

Porous electrodes are ubiquitous in electrochemical technologies including energy storage, water desalination, and electrocatalysis. Porous electrodes may be formed out of one material or as a composite of two or more materials to provide additional functionality (e.g. photosensitivity, redox activity, catalytic activity, etc.). Examples of porous electrodes formed from one material include porous carbon electrodes¹⁻³ or metal foams^{4,5} that are used in supercapacitors, ^{6,7} and capacitive deionization.^{8–10} Examples of porous composite electrodes include Li-ion battery cathodes, ^{11,12} battery deionization electrodes, 13-15 redox flow battery electrodes, 16 and electrodes for electrocatalysis. 17-19 The rationale for employing porous composite electrodes typically arises from a desire to increase the interfacial surface area between an active solid phase and the electrolyte, where electrodes with higher porosity and smaller pore diameters maximize the interfacial contact area with the electrolyte. For example, in catalysis, porous electrodes decorated with small catalyst particles maximize the surface area of catalyst exposed to the electrolyte to increase catalyst activity. Similarly, in Li-ion battery or battery deionization electrodes, higher electrode porosity and smaller pore diameters increase the surface area of active material exposed to the liquid electrolyte, providing an interconnected network of liquid-phase electrolyte deliver ions to/from redox-active domains.

However, although higher electrode porosities and smaller pore diameters are employed to provide greater interfacial contact area with the electrolyte phase, these factors also necessarily increase the length scales for liquid phase diffusion for the same electrode mass. By way of example, we estimate the relative impact of these parameters on the diffusion length scales in a simple model porous electrode geometry in the Supporting Information (SI). We find that an increase from 40% to 60% porosity at a constant electrode mass and top-down cross-sectional area leads to a 50% thicker electrode (SI Section A). Similarly, reducing the pore diameter by a factor of two at constant electrode mass and porosity leads to a four-fold increase in the total path length of pores within the electrode volume (SI Section B). We find that increasing porosity and decreasing pore diameter both lead to larger fractional increases in these diffusion length scales (electrode thickness and total pore path length) than the corresponding fractional increases in the surface area in contact with the electrolyte phase (SI Section C). The qualitative impact of these variables in a simple model system motivates the need to consider diffusion limitations in electrode design.

In addition to higher porosities and smaller pore diameters leading to increasing diffusion path lengths within pores, nanoscale pore geometries also introduce confinement effects that influence electrode charging physics.^{20–22} Nanoscale confinement in electrode pores of < 100 nm in diameter leads to electric-double-layer overlap and alters molecular transport, electron transfer, solvent dielectric properties, and adsorption behavior. 20-22 These effects can further limit the energy efficiency of electrochemical processes. Electrode porosity therefore presents a conundrum for electrode design – to increase the surface area of the electrode, higher porosities and smaller pore diameters are desired; however, these higher porosities and smaller pores expand the electrode volume, introduce longer length scales for diffusion, and generate unwanted nanoconfinement effects, thereby reducing the effectiveness of these electrodes. Following previous work, ^{23,24} we employ the potential-dependent Thiele Modulus²⁴ in SI Section D to estimate the net effect that that diffusion limitations have on the efficiency of electrochemical processes. We find that for typical, composite battery cathodes^{11,12,25,26} and metal foam electrodes⁵ >75% of the electrode volume experiences diffusion limitations that limit electrode rate capability, and that an even larger fraction of the volume of macroscale porous carbon foams²⁷ is restricted by diffusion. We note that a typical composite battery cathode has a porosity of ~20-60%, average pore dimeters of ~200 nm, and a composite active material thickness of ~100 um. 11,12,25,26 This is in contrast to carbon and metal foams, which have 70-99% porosity, 5,27 average pore diameters for mesoporous carbon foams of ~20 nm ^{27,28} and up to ~1 mm in metal foams, ⁵ and electrode thicknesses of 2-20 mm. ^{5,27}

To address the diffusion limitations outlined above that are inherent to porous electrodes, it is appealing to consider mechanically compressible porous electrodes. A compressible electrode with a high porosity and larger pore diameters provides open channels that prevent negative effects from nanoscale confinement, and mechanical compression of the porous structure allows for convective exchange of ions from the surrounding electrolyte, eliminating diffusion limitations. Previous work has generated compressible carbon sponge electrodes using freeze drying, ²⁹ supercritical drying, ³⁰ CVD, ^{31,32} and 3D printing. ³³ These carbon foams can then be modified post-synthesis by decorating or coating with additional functional material to enhance redox activity. ³⁴ However, current methods for carbon foam synthesis provide limited control over the porosity and pore size distribution of these foams. Another approach has been to employ commercially available polymer foams and deliver electrically conductive coatings, for example via solution casting. ^{37–42} However, previous methods of delivering conductive coatings provided poor control

over the thickness and uniformity of the coatings onto the sponge supports, requiring thicker polymer coatings to achieve electrical connectivity, and thereby limiting the mechanical compressibility of these conductive foams. In the present work, we aim to establish a synthesis approach to form a composite polymer foam electrode using commercially available polyurethane (PU) foam supports coated with uniform and conformal electrically conductive and redox-active polymer coatings. Here, our goal is to establish a synthesis platform to independently control the foam porosity/pore volume and the thickness of the redox-active coatings of compressible electrodes. This work builds off prior work using vapor phase infiltration (VPI) to modify polymer foams with inorganic coatings deposited by sequential gas-phase exposures of organometallic precursors and water in a scheme similar to atomic layer deposition (ALD). 43-46 Here, instead of inorganic coating chemistries used previously, we deliver electrically conductive polymer coatings. We employ oxidative molecular layer deposition (oMLD) of poly(3,4 ethylenedioxythiophene) (PEDOT) using sequential gas-phase precursor exposures of 3,4 ethylenedioxythiophene (EDOT) and molybdenum pentachloride (MoCl₅). 47,48 PEDOT formed by oMLD has been found in prior work to exhibit electrical conductivities in excess of 6000 S/cm,⁴⁹ and electrochemical charge storage capacities in excess of up to 120 mAh/g.⁵⁰

III. Experimental Methods

Oxidative molecular layer deposition (oMLD) was performed using a custom hot-walled viscous flow reactor described previously.^{51,52} Open–cell 1" cube PU sponges with a density of 1.6 lb/ft³ (McMaster-Carr) were used as sponge substrates. Deposition of PEDOT thin films by oMLD was accomplished based on previously established growth conditions.^{48,53} Using PID temperature controllers, the temperature of the oMLD reactor chamber was fixed at 150°C. Ultra-high purity argon carrier gas (Ar, Airgas) flowed continuously into the reactor chamber at a total flow rate of 250 SCCM and pressure of 0.85 Torr. Molybdenum pentachloride (MoCl₅, 99.6%, Fischer Scientific) and Ethylenedioxythiophene (EDOT, 98%, 1PlusChem) used for PEDOT oMLD growth were both kept at a fixed temperature of 100 °C using jacketed flow-over precursor bubblers with PID temperature control. The precursors were used as-received and were transferred into the precursor delivery bubblers in an argon-filled glovebox. Under these growth conditions, a peak dose pressure of ~100 mTorr higher than base pressure was observed for EDOT. The sample tray was passivated with the oMLD PEDOT chemistry before deposition on PU Sponges. Si wafers (Silicon Valley Microelectronics) were placed on either side (both upsteam and downstream) of

each sponge on the tray during oMLD growth. One oMLD cycle consisted of (A) a MoCl₅ dose, (B) carrier gas purge, (C) EDOT dose, and (D) carrier gas purge. As described below, the timing of precursor and purge steps were adjusted to optimize growth onto the PU sponge substrates.

Mechanical Compression Testing of PU sponges was performed with a motorized test stand (ESM303-Mark-10) equipped with a force gauge (M5-100, Series 5 Advanced Digital Force Gauge, 100 lbF). Graphite rods of 1" diameter were connected to (a) the base of the test stand and (b) the force gauge attached to the motorized stage. These graphite rods were connected to the housing using plastic fittings to electrically isolate the graphite rods and allow for electrical characterization during mechanical compression/decompression. All mechanical compression was performed at a constant strain rate of 0.1 in/min. PU sponges were compressed up to 0.5" (50% strain). To acquire the values of load versus strain the MESURgauge Plus software by Mark-10 was used. Electrical resistance data was measured simultaneously using a potentiostat, as described below.

<u>Electrical Impedance Spectroscopy (EIS)</u> was performed on sponges to measure the electrical impedance (Z) of the sponge as a function of AC frequency (f) using a Biologic SP-150 potentiostat. These measurements were performed in two modes of operation.

In the first mode of measurement, the electrical impedance across the PEDOT-coated PU sponges was measured during mechanical testing using electrical contacts on two ends of the fully intact sponge (see above). For this, the graphite rods used for mechanical compression testing were electrically connected to a potentiostat using a copper wire attached to a stainless steel set-screw in contact with each graphite rod. EIS experiments were performed over a frequency range of 500 mHz to 1 MHz at an amplitude of 10mV. The x intercept of Nyquist admittance plots at low frequency (100 Hz) from these measurements was used to report real impedance below.

In the second mode of measurement, sponges were cut in half and electrical contact was made at two points on the inner surface of one half of the sponge within the approximate center of the original PU sponge cube, such that the EIS measurements could be used as a metric for the connectivity of the PEDOT coating throughout the bulk of the sponge. For this mode of measurement, two Keven probe micropositioners equipped with 125 µm diameter beryllium copper alloy probe tips were positioned at either (a) the center and one edge, or (b) opposite edges

of the internal surface of the coated PU sponges, and the electrical impedance behavior was compared between these two configurations.

Raman Spectroscopy was conducted with a Renishaw in Via Raman spectrometer with 633 nm excitation laser. Data was collected over 600–3000 cm⁻¹ with a sweeping scan rate of 10 cm⁻¹ s⁻¹ and a laser power of 10.1 mW. Due to difficulties in acquiring Raman data on the microporous PU sponges arising from diffuse scattering, 1/16" thick solid nonporous sheets of 95A durometer PU (McMaster Carr) were used as surrogates for the solid fibers of the PU sponge to assess how MoCl₅ impacts the chemical structure of PU. PU sheets were analyzed by Raman Spectroscopy before and after exposure to gas phase MoCl₅ at 150 °C.

X-ray photoelectron spectroscopy (XPS) was also performed on 1/16" thick solid PU sheets before and after exposure to gas phase MoCl₅ at 150 °C. XPS data was acquired using a Thermo Scientific Nexsa instrument with a monochromatic Al X-ray source. Survey scans employed a 400 μm X-ray beam using constant analyzer energies of 200 eV, respectively. All peaks were charge corrected by shifting the C 1s peak of all spectrums at an energy of 284.8 eV.

Spectroscopic Ellipsometry was used to assess PEDOT film thickness on Si wafer samples using a J.A. Wollam Alpha-SE ellipsometer at wavelengths of between 380-890 nm at an incident angle 65°. SE data analysis and modeling were performed using the CompleteEASE software package. PEDOT films were fit using three Lorentz oscillators^{54–56} centered at 0.049 eV, 3.1 eV, and 4.2 eV. Here, Lorentz oscillators were used instead of the Cauchy model described previously for oMLD PEDOT⁵⁰ due to the shorter purge times (*vide infra*) which evidently produced PEDOT at a different state of charge compared to this prior work.

Scanning Electron Microscopy (SEM) was carried out using an FEI Quanta 600F operated in high vacuum at an accelerating voltage of 10 kV. Each sponge to be imaged by SEM was cut in half and SEM images were acquired from the inner surface of one half of the sponge, such that the SEM images represent the approximate center of the original PU sponge cube. Wide field images were collected at 35x (HFW=3.66mm), and individual fibers imaged at 500x (HFW=256μm). Energy Dispersive x-ray Spectroscopy (EDS) mapping was performed at 10kV.

IV. Results and Discussion.

Effect of MoCl₅ Dose Time on Electrical Properties

The foundational hypothesis motivating our effort here to employ oMLD to deliver PEDOT coatings on PU sponges is that the sequential self-limiting precursor exposures used in oMLD will allow for the formation of a uniform and contiguous network of electrically conducting PEDOT within PU sponges. We expect that this will enhance electrical conductivity relative to wetchemical methods for delivering PEDOT onto PU foams. As an initial test, we coated PU sponges with 150 oMLD cycles of PEDOT using 10 s EDOT dose time, 100 s MoCl₅ dose time, and 100 s Ar purge after each precursor dose. These growth conditions were established in previous work and found to provide saturating doses on flat substrates.⁴⁸ After forming the PEDOT-coated PU sponge using oMLD, we employed electrical impedance spectroscopy (EIS) to measure the electrical impedance (Z) of the sponge as a function of AC frequency (f), as depicted in Figure 1. These measurements were performed under ~10% strain using 1" diameter graphite rod contacts as described in the Experimental Methods Section.

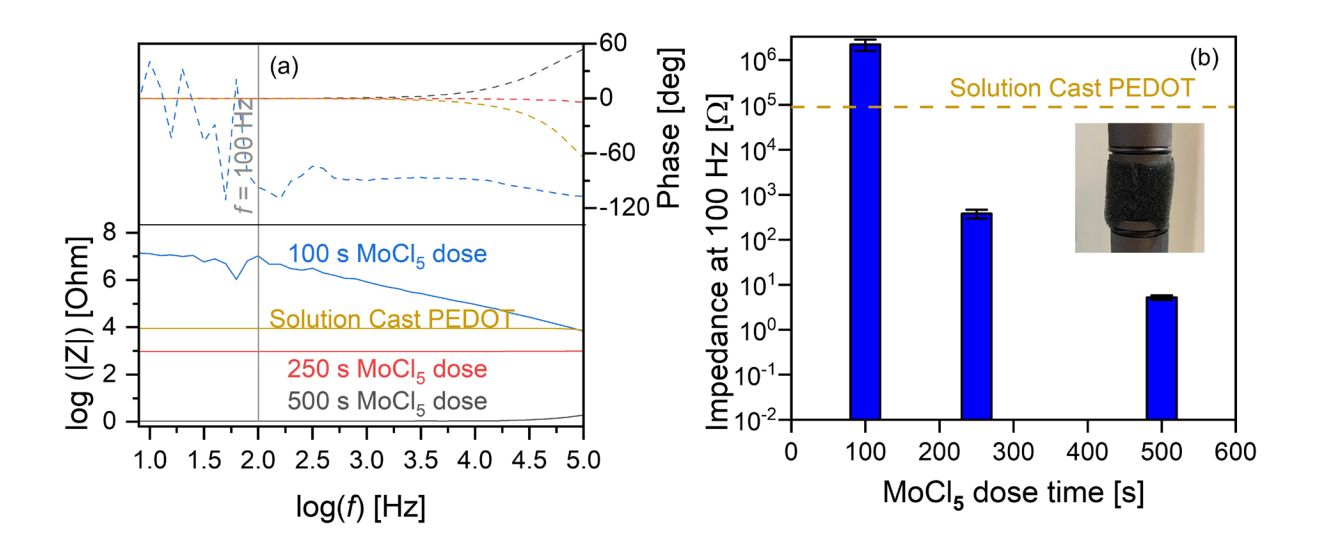


Figure 1. Electrical impedance of PU foams coated using. 150 oMLD cycles of MoCl₅/EDOT at 150 °C using MoCl₅ dose times of 100 s, 250 s, and 500 s, compared with solution cast PEDOT coatings, including (a) Bode plot indicating resistive behavior at f < 100 Hz and (b) impedance of each sample from (a) as measured at f=100 Hz.

The Bode plot of the EIS data in Figure 1a for the 100 s MoCl₅ dose time condition in Figure 1a indicates a high impedance of $Z > 10^6 \Omega$ at low $f \le 100$ Hz. We expect that this high electrical impedance arises because MoCl₅ precursor delivery is insufficient to saturate the full surface area of the PU sponge. The MoCl₅ vapor pressure is <10 mTorr, requiring a ≥ 100 s dose time for

complete saturation on flat substrates.⁴⁸ By increasing the MoCl₅ exposure using 250 s and 500 s MoCl₅ dose times, we observe a decrease in Z to 10^3 Ω and <10 Ω , respectively, at low $f \le 100$ Hz, confirming that an increased MoCl₅ dose time provides a more complete PEDOT coating within the PU foam substrate. We note that ideal resistive behavior (phase equals zero) is observed for $f < 10^3$ Hz for the solution cast PEDOT, and 250 s and 500 s MoCl₅ dose time conditions, and the total impedance plateaus to a constant value for $f \le 100$. As such, we employed a frequency of 100 Hz for further electrical impedance characterization below, unless otherwise noted.

In Figure 1b, we compare the electrical impedance as measured at f = 100 Hz for each of the three samples in Figure 1a relative to a PU sponge coated using solution cast PEDOT. Here, the solution casting of PEDOT onto the PU sponge was performed by mixing EDOT monomers and the MoCl₅ oxidant in an ethanol solution containing a PU sponge following procedures described previously.⁵⁷ Despite the solution-cast PEDOT forming a visible amount of excess PEDOT on the PU sponge, the electrical impedance we measured for this coating approach was still high at $8.9 \times 10^4 \Omega$. By contrast, the 500 s MoCl₅ dose condition yielded an electrical impedance of 5.2Ω when measured under the same conditions. The 500 s MoCl₅ dose condition produced a resistance 1.7×10^4 times smaller than using solution casting. This provided an initial positive indication that improving the conformality and uniformity of PEDOT coatings using oMLD could enhance the electrical conductivity of the PU sponges beyond solution casting and may provide a pathway for us to generate porous, electrically conductive electrodes with controlled microstructure.

Effect of MoCl₅ Dose Time on Mechanical Properties

In a next step, we set out to confirm that the mechanical properties of the PU were not significantly altered by the oMLD PEDOT coating. For this, we employed a mechanical compression tester to measure stress (σ) vs. strain (ε) up to 50% compression (ε=0.5) for sponges formed using the same oMLD conditions as in Figure 1. Unfortunately, here we identified a significant deficiency in mechanical properties when using the 500 s MoCl₅ dose time to deliver oMLD PEDOT. Presented in Figure 2a and 2b are photographs taken during the mechanical compression of sponges coated using 100 s and 500 s MoCl₅ dose times, respectively. In each panel (a and b) of Figure 1, we depict photographs of the (i) initial sponge before compression followed by (ii-iv) sequential compression up to 50% strain, and then (v) a final photograph of the sponge after removing compression. The PU sponge coated using a 100 s MoCl₅ dose time behaved qualitatively like an

uncoated sponge – returning to its original shape after compression. By contrast, the PU sponge coated using a 500 s MoCl₅ dose time crumbled under applied stress, disintegrating into a course powder after mechanical compression, as depicted in Figure 2b.v. The highest measured pressures under 50% compression were 1.52 psi and 4.72 psi in Figure 2a and Figure 2b, respectively.

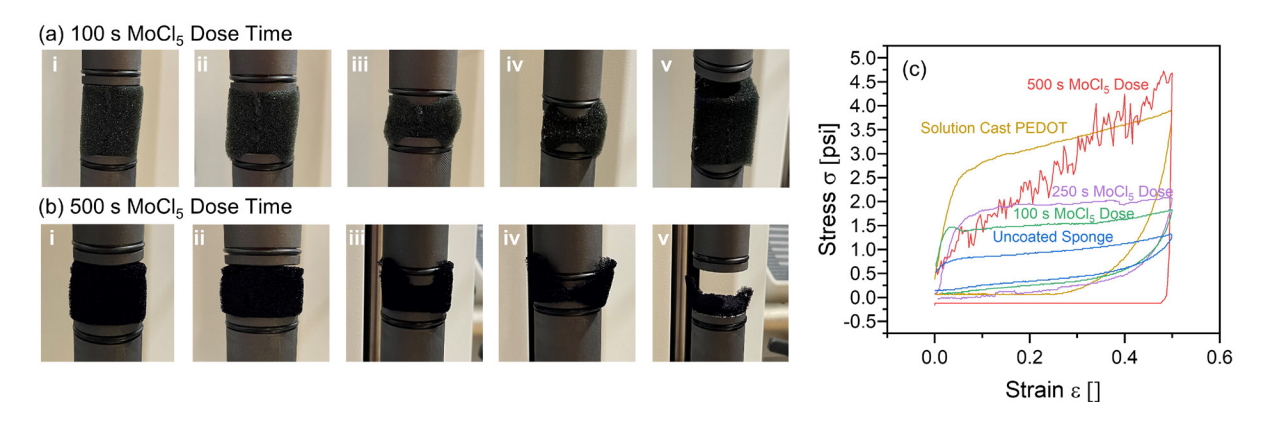


Figure 2. PEDOT-coated PU sponges formed using a (a) 100 s MoCl₅ dose time during oMLD growth recover their shape after mechanical compression (i-iv) and release (v), however, after using a (b) 500 s MoCl₅ dose time, mechanical compression (i-iv) disintegrates the sponge and the sponge does not recover its shape after release (v). This qualitative behavior is consistent with (c) mechanical stress-strain testing using a strain rate of 0.1 in/min for bare PU sponges, where a 500 s MoCl₅ dose time leads to a mechanically brittle sponge, unlike the shape recovery behavior observed for bare PU sponge, solution-cast PEDOT-coated PU sponge, and oMLD PEDOT-coated PU sponge.

To further quantify this mechanical compression behavior, in Figure 2c we plot σ vs. ϵ data collected during mechanical compression of PU sponges with PEDOT coatings delivered by oMLD using 100, 250, and 500 s MoCl₅ dose times, and compare this vs mechanical compression data collected for uncoated PU sponge and PU sponge coated with PEDOT using solution casting. In these graphs, ϵ =0 corresponds to the uncompressed state. As the sponge is compressed (ϵ increases) at a constant strain rate of 0.1 in/min, the increase in the necessary stress required to compress the sponge is measured using a force gauge. The uncoated PU sponge reflects typical behavior for an open-cell compressible foam, where the stress initially rises as the sponge fibers undergo elastic deformation. Under sufficient stress, the fibers yield, leading to bulk collapse of the porous foam network, producing a region of relatively constant stress over a wide range of strain (e.g. from $0.1 < \epsilon < 0.4$). After reaching 50% strain, the strain is gradually removed at the

same strain rate of 0.1 in/min, and the measured stress reflects the force that the sponge delivers to the piston under decompression. Except for the PU foam coated with 500 s MoCl₅ dose time, we observe qualitatively similar σ vs. ε curve shapes for all of the sponges in Figure 2c, consistent with open-cell foam collapse. The PU sponges coated with oMLD PEDOT using 100 s and 250 s MoCl₅ dose times exhibit average stresses of 1.52 ± 0.05 psi and 1.94 ± 0.05 psi, respectively over the range in strains from $0.1 \le \varepsilon \le 0.4$, compared with 0.96 ± 0.08 psi for the uncoated sponge and 3.2 ± 0.2 psi for the PU sponge with a solution-cast PEDOT coating. Likewise, the slope in σ vs. ε on onloading indicates a Young's modulus of 27 ± 1 psi and 35 ± 2 psi, for the 100 s and 250 s MoCl₅ dose times, respectively, compared with 12.7 ± 0.6 psi for the uncoated sponge and 63 ± 3 psi for the PU sponge with a solution-cast PEDOT coating. By contrast, the PU sponge coated with oMLD PEDOT using a 500 s dose time exhibits a linear increase in stress on compression consistent with the disintegration of the foam fibers. After reaching the maximum strain of 0.5, this sponge exerts no force on the pistons during decompression, which is expected considering the crumbled powder remnants we observe in Figure 2b.v after compression.

We expect that PU becomes brittle under long MoCl₅ because of oxidative chemical decomposition.⁵⁸⁻⁶⁰ PU is known to degrade under oxidizing environments and elevated temperatures. Under these conditions, urethane groups oxidize to form isocyanate and aldehyde products.⁵⁸ We expect a similar pathway proceeds here, where MoCl₅ oxidizes urethane groups according to R_1 -NH-CO₂-C- R_2 + MoCl₅ \rightarrow R_1 -N=C=O and O=CH- R_2 + 2HCl + MoCl₃, breaking down the PU chemical structure into volatile decomposition byproducts. We note that Cl₂ is known to decompose PU,61 and the MoCl₅ oxidant undergoes a two-step reduction of MoCl₅→MoCl₄→MoCl₃ with oxidation potentials of 3.34 V and 1.46 V vs. SHE,⁴⁸ both of stronger oxidation potential than Cl₂ (1.36 V vs. SHE). To confirm that MoCl₅ is leading to decomposition of the PU chemical structure, we exposed 1/16" thick dense polyurethane sheets to a prolonged (1000 s) MoCl₅ exposure (no EDOT dose) and performed XPS and Raman spectroscopy to measure the chemical composition before and after MoCl₅ exposure. After MoCl₅ exposure, we observed a macroscopically visible roughening and discoloration of the PU sheet, indicating that MoCl₅ is chemically degrading PU, consistent with our expectations. Using XPS and Raman spectroscopy, we expected to see a decrease in C-O and C=O groups comprising the ester-like group within the urethane based on the mechanism proposed above. Indeed, XPS results in Figure 3a indicate a decrease in peak intensity at C 1s binding energies of ~286 and ~289 eV,

consistent with the removal of C-O and C=O, respectively. Likewise, the Raman spectra in Figure 3b indicate a decrease in the ester C=O feature at 1732 cm⁻¹ after MoCl₅ exposure.^{62–64} We also observe a decrease in the Raman intensity at 1530 cm⁻¹ after MoCl₅ exposure, corresponding to loss of C-N and N-H groups.^{62–64} We note that we observe equivalent peak intensity for C-H modes at 1300 cm⁻¹ and 2800-3000 cm⁻¹, and CH₂ modes at 1443 cm⁻¹ before and after MoCl₅ exposure indicating that these decreases in ester and N-H do not arise from different sampling volumes.^{62–64} These data support that MoCl₅ oxidatively decomposes polyurethane, leading to the mechanical brittleness we observe under high MoCl₅ exposure in Figure 2.

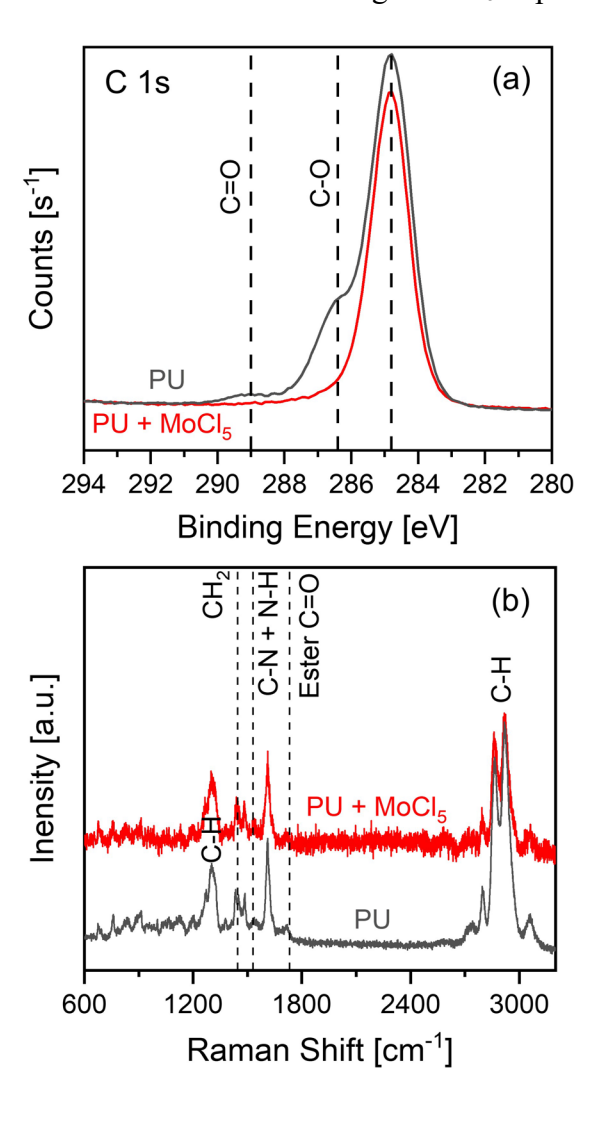


Figure 3. (a) XPS and (b) Raman spectroscopy of PU before and after 1000 s MoCl₅ exposure at 150 °C indicating oxidative decomposition of urethane groups from MoCl₅ exposure.

Effect of EDOT Purge Time on Mechanical Properties

Unfortunately, the chemical reaction of MoCl₅ with PU makes it difficult to coat PU sponges with PEDOT by oMLD because MoCl₅ or another strong chemical oxidant is needed to polymerize EDOT.⁴⁸ We can decrease the MoCl₅ dose to limit PU degradation and preserve the PU sponge mechanical properties as indicated in Figure 2, but this leads to higher electrical resistance through the sponge, as shown in Figure 1. Considering these constraints, we hypothesized that decreasing the purge times following each precursor dose may overcome these challenges. Our rationale for this approach arose from previous studies examining the effect of purge time on MLD growth processes^{53,65} and the effect of purge time on atomic layer deposition (ALD) within polymer substrates. 43-46,66 In general across these processes, vapor phase precursors are known to dissolve and infiltrate into bulk polymers, requiring 100s of seconds or more of purge time to fully remove loosely bound precursors from the bulk polymer structure. Even on rigid dense substrates (e.g. Si), MLD purge times below 100 s lead to an increase in polymer growth rate, either from a similar dissolution effect into the bulk MLD film or from the formation of multilayers of monomer on the growth surface. 53,65 Considering these known phenomena, we expect that an excess of EDOT monomer accumulates either on the surface of the PU or dissolved within the PU bulk during the EDOT dose, and that this EDOT slowly dissipates during the purge step. By decreasing the purge time after the EDOT dose, our strategy was to use this excess EDOT as a transient protective layer that would react with the MoCl₅ oxidant and rapidly form a surface PEDOT layer, preventing MoCl₅ from arriving at the underlying PU substrate. In other words, our goal was to intentionally perform controlled chemical vapor deposition (CVD) to direct the polymerization to the surface of the PU fibers rather than within the PU fibers.

To evaluate whether this approach would be viable, we reduced the EDOT purge time from 100 s to 60, 30, 20, and 15 s, keeping the number of oMLD cycles constant at 30 for deposition onto PU. The mechanical properties for these PU sponges treated using different purge times during PEDOT oMLD are reported in Figure 4. The mechanical testing data under compression (σ vs. ϵ) is depicted in Figure 4a for each of these purge conditions, compared with an uncoated PU sponge and a PU sponge coated with PEDOT using solution casting. We find that the PU sponge coated with oMLD PEDOT using a 20 s EDOT purge time exhibits a qualitatively similar σ vs. ϵ curve, where a roughly constant value of stress is measured with increasing strain. This is consistent with bulk foam pore collapse similar to the mechanical behavior observed for uncoated PU and PU

coated with PEDOT using solution casting in Figure 2a. In contrast, we find that sponges formed using 60, 30, and 15 s purge times exhibit increasing stress with increasing strain, which may indicate a gradient in mechanical properties throughout the foam. In Figure 4b we plot the average stress (σ_{avg}) measured over the range $0.1 \le \epsilon \le 0.4$ for each of these sponges. We measure $\sigma_{avg} = 0.96 \pm 0.08$ psi for uncoated PU and $\sigma_{avg} = 3.2 \pm 0.02$ psi for PU coated with PEDOT using solution casting. The values of σ_{avg} fall between these bounds for all the oMLD-coated PEDOT sponges, with the highest value of $\sigma_{avg} = 2.1 \pm 0.1$ psi measured for the 20 s EDOT purge time. We expect this higher value of σ_{avg} for the 20 s EDOT purge time arises from an increased PEDOT thickness on the fibers from CVD reactions (*vide infra*). Even for the 20 s purge condition, the value of stress to collapse the foam is 38% lower than the stress required to collapse the PU foam coated with PEDOT using solution casting. The error bars in Figure 4b are the standard deviation in σ averaged over the range $0.1 \le \epsilon \le 0.4$, and we observe a higher variance in sponges coated using 15, 30, and 60 s EDOT purge times, consistent with the graded σ vs. ε curve measured in Figure 4a for these growth conditions.

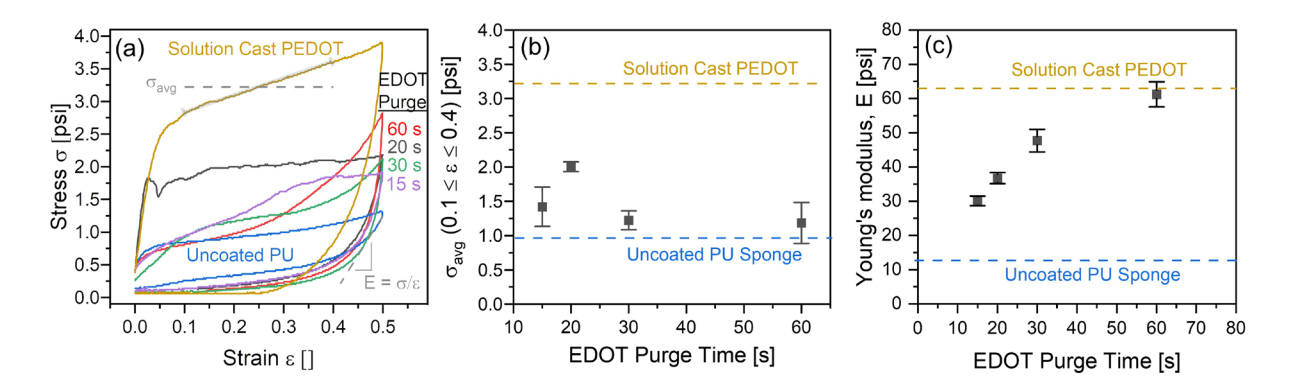


Figure 4. Effect of EDOT purge time on the mechanical properties of PEDOT-coated PU formed using 30 oMLD cycles of EDOT/MoCl₅, including (a) stress vs. strain during compression at a strain rate of 0.1 in/min, (b) σ_{avg} on compression measured over $0.1 \le \epsilon \le 0.4$ from (a) vs. EDOT purge time, and (c) Young's modulus on decompression from (a) vs. EDOT purge time.

In Figure 4c we plot the Young's modulus, E, on decompression for each of the sponges depicted in Figure 4a. We measure $E = 12.7 \pm 0.6$ psi for uncoated PU and $E = 63 \pm 3$ psi for PU coated with PEDOT using solution casting. The values of E fall between these bounds for all the oMLD-coated PEDOT sponges, starting at with a value of $E = 30 \pm 1$ psi using a 15 s EDOT purge time up to a value of $E = 61 \pm 4$ psi using a 60 s purge time. We measure a value of $E = 37 \pm 2$ psi for

the 20 s EDOT purge time condition, which is a factor of \sim 3 higher than the uncoated PU. The value of error bars in Figure 4c represent the standard error in the slope of σ vs. ϵ on decompression from least squares linear regression. The trend in Young's modulus vs. EDOT purge time in Figure 4c is consistent with our expectations based on the reaction of MoCl₅ with the PU fibers as outlined in Figure 3. At higher EDOT purge times, more of the EDOT is removed from the PU fibers, and the MoCl₅ readily degrades the PU, leading to increased brittleness of the fibers. As the purge time is decreased, the EDOT molecules remaining on/within the PU act as a reactive barrier preventing MoCl₅ from reacting with and degrading the PU. These results confirm our hypothesis that decreasing the purge time following the EDOT dose will prevent reaction of MoCl₅ with the PU fibers, making the PEDOT-coated PU foam softer.

Effect of EDOT Purge Time on Electrical Properties

As a side-effect of decreasing the EDOT purge time to prevent MoCl₅ from reacting with the PU fibers, we would expect that this will also lead to an increased PEDOT film thickness due to a greater extent of vapor-phase (CVD) reaction between EDOT and MoCl₅. To examine this, we measured the thickness of PEDOT formed on Si wafers placed adjacent to the foam pieces within the reactor, as well as the electrical resistance across the foam pieces under ~10% mechanical compression, as plotted in Figure 5. Indeed, we find that starting from an EDOT purge time of 120 s down to a purge time of 30 s, the PEDOT film thickness on Si increases from 19 ± 2 nm at 120 s EDOT purge time to 120 ± 20 nm at 30 s EDOT purge time. For an EDOT purge time of 20 s and 15 s, the film thickness drops to 50 ± 8 nm and 14.0 ± 1 nm. Here the error bars in thickness represent the standard deviations measured on two Si wafers positioned upstream and downstream of the PU sponge in the oMLD reactor. We note that the EDOT and MoCl₅ precursors do not only react at the surface of the PU sponge fibers, but infiltrate into the bulk PU fibers down to a depth of 8 µm (vide infra). Therefore, the thicknesses on Si wafers adjacent to the PU sponges are not a direct indication of the amount of PEDOT deposited on/into the PU sponge. We report the PEDOT thicknesses on Si wafers placed adjacent to the PU here to help describe the qualitative effect of EDOT purge time on PEDOT oMLD growth.

Considering this, the high variation in film thickness upstream and downstream of the PU for the 30 s purge time may arise from either (a) a thickness gradient due to CVD-type reactions or (b) decomposition of the PU sponge, leading to outgassing of decomposition byproducts that may

condense on the Si adjacent to the PU sponge. Raman spectroscopy performed on Si wafers placed both upstream and downstream of the PU sponge coated using a 30 s purge time (not shown) does not provide evidence of PU residue present on either sample, indicating that the higher thickness value downstream of the PU is related to a thickness gradient due to CVD-type reactions. We emphasize that the absence of PU Raman signal in the Si downstream of the PU sponge for the 30 s purge time does not imply that the PU did not decompose, but only that PU decomposition byproducts did not incorporate into the film that formed on the downstream Si. A longer EDOT purge time is expected to yield more PU decomposition and less CVD reaction, while a shorter EDOT purge time is expected to yield less PU decomposition and more CVD reaction. Furthermore, the higher PEDOT thickness and larger variation in thickness for the 30 s purge time vs. the 20 s purge time suggests a higher vapor phase EDOT concentration after 30 s purge than 20 s of purge. This indicates that more EDOT has escaped from the PU at the longer 30 s purge time, which is consistent with less PEDOT deposited on the PU for the 30 s purge time vs. the 20 s purge time, consistent with the lowest electrical resistance measured for a 20 s purge time in Figure 5.

We attribute the decrease in PEDOT thickness at a 15 s purge to the gas-phase mixing of precursors upstream of the sponge, limiting precursor delivery to the sponge. The trend in thickness vs. EDOT purge time is generally consistent with the electrical properties, where the lower electrical resistance is measured on sponges where a thicker PEDOT film is observed on Si witness wafers. We interpret that the lowest electrical resistance measured using a 20 s EDOT purge arises from effectively balancing PEDOT deposition with limited PU decomposition, consistent with the largest increase in mechanical properties using a 20 s EDOT purge as reported in Figure 4, where the 20 s EDOT purge yields the highest average stress during bulk foam collapse.

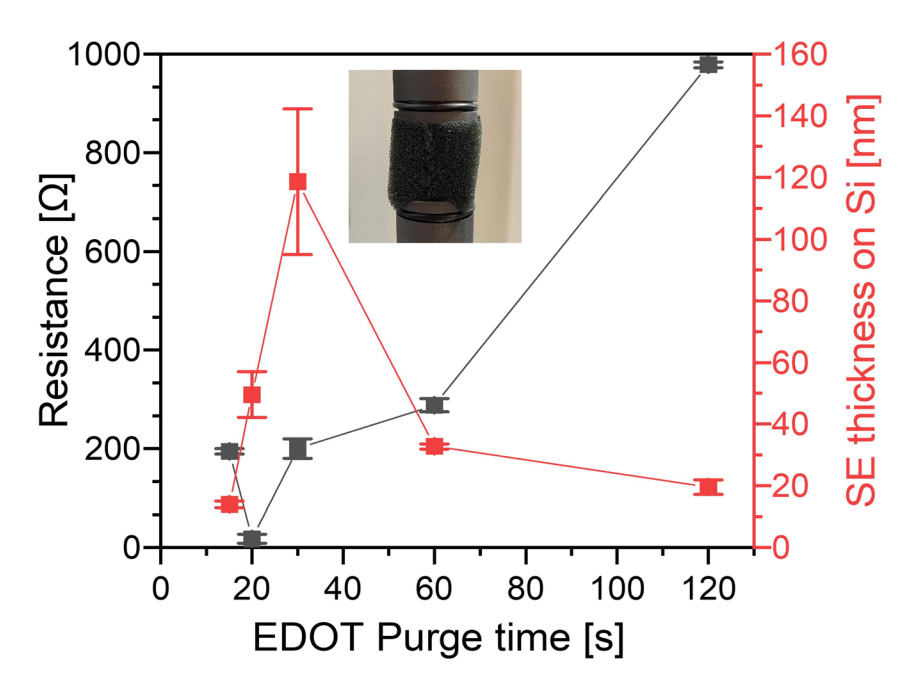


Figure 5. Effect of EDOT purge time after 30 oMLD cycles of EDOT/MoCl₅ on the resistance measured on a 1" foam cube (left axis) and the average thickness measured on two Si wafers placed upstream and downstream of the foam pieces (right axis).

Taken together, the results in Figures 4 and 5 suggest that a 20 s EDOT purge time is most viable for forming PEDOT films onto PU sponges using oMLD of the purge times tested – this purge time resulted in mechanical properties consistent with bulk foam collapse in Figure 4a, the lowest electrical resistance in Figure 5, and moderate increases in the average stress and Young's Modulus values of ~2 times and ~3 times higher, respectively, than uncoated PU foam in Figure 4b and 4c. However, to be viable in generating porous electrodes, the oMLD PEDOT coatings must uniformly coat the PU sponge through to the center of each foam piece.

Effect of oMLD Cycles on PEDOT Uniformity and PU Properties

To examine the depth to which PEDOT was formed within the PU foams, we sliced each foam piece in half and employed Kelvin-probe micropositioners to measure the electrical resistance from the center of the sponge to the outside edge (Figure 6a,b) vs. from one outside edge to the opposite outside edge (Figure 6c,d). We plot the resistance measured using each of these configurations as a function of the number of EDOT/MoCl₅ oMLD cycles in Figure 6e. For these, and all further experiments below, we employed the optimized growth conditions of a 20 s EDOT dose, 20 s EDOT purge, 500 s MoCl₅ dose, and 20 s MoCl₅ purge based on the data in Figures 1,

4, and 5, and we varied the number of oMLD cycles from 10 to 100. The center-to-edge and edge-to-edge resistance values measured for 1" foams formed using each of these conditions are plotted in Figure 6.

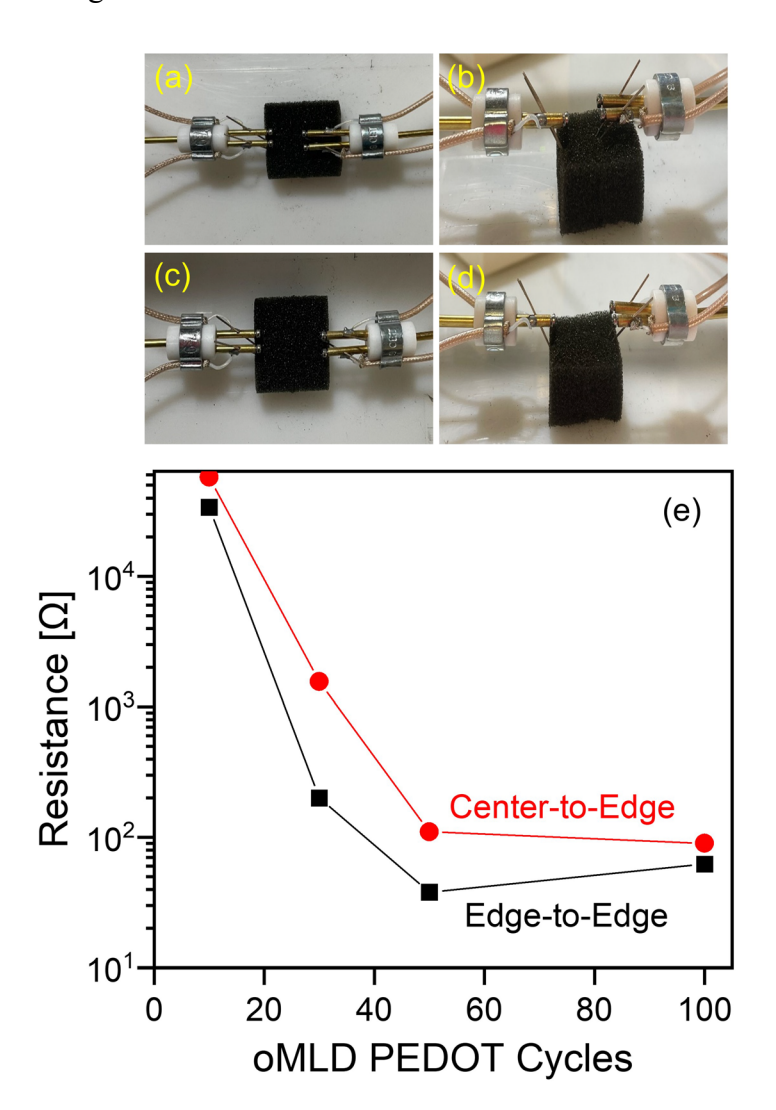


Figure 6. 1" PU foams coated with oMLD-PEDOT were sliced in half and micropositioner Kelvin probes were placed in center-to-edge configurations as shown from the top (a) and side (b), as well as in edge-to-edge configurations as shown from the top (c) and side (d), and the electrical resistance was measured in each of these configurations (e).

Here, as we increase the number of oMLD cycles from 10 to 50, we observe a decrease in the electrical resistance by ~3 orders of magnitude for both the center-to-edge and edge-to-edge measurement conditions. We attribute this decrease in resistance to an increase in PEDOT thickness/loading with an increasing number of cycles. A greater amount of PEDOT material will

increase the electrically conductive network throughout the PU fibers, and thereby reduce the electrical resistance of the sponge. We observe roughly the same electrical resistance for both 50 and 100 oMLD cycles, suggesting that additional material provides diminishing returns in electrical connectivity after ~50 oMLD cycles. This may arise in part from residual oxidation of the PU as described in Figure 3 as the number of oMLD cycles increases (i.e. higher total MoCl₅ exposure). To first order, one would expect that the electrical resistance for center-to-edge would be $\sim 1/2$ of the electrical resistance for edge-to-edge, neglecting differences in the foam network that may impact electron conduction pathways. However, the center-to-edge electrical resistance is 2-8 times higher than the edge-to-edge electrical resistance for all numbers of oMLD cycles in Figure 6. This suggests that the electrical connectivity pathways may not be as robust to the center of the sponge as around the external perimeter of the sponge, consistent with the partial CVD growth at this purge time as discussed above surrounding Figure 5. Nonetheless, the general trend in electrical resistance vs. number of oMLD cycles and the order-of-magnitude values of electrical resistance for center-to-edge tracks closely with the values measured for edge-to-edge, indicating that the PEDOT film is delivered all the way to the center of the sponge, and that increasing number of oMLD cycles increases the thickness/loading of PEDOT throughout the whole volume of the PU sponge.

To further confirm PEDOT loading at the center of each 1" foam cube, we performed SEM measurements on the center area of the PU sponges in Figure 6 after cutting them in half. In Figure 7, we show SEM micrographs of PU sponges coated with 30 oMLD cycles (a-c), 50 oMLD cycles (d), and 100 oMLD cycles (e). All samples in Figure 7 were formed using a 20 s EDOT dose, 20 s EDOT purge, 500 s MoCl₅ dose, and 20 s MoCl₅ purge based on the studies in Figures 1, 4, and 5 above. The SEM images in panels a, d, and e of Figure 7 were collected using backscatter electron detection (BSD) while carefully maintaining identical conditions (beam current, working distance, acquisition time, and detector brightness and contrast). By controlling the portion of the signal yield attributable to variable system parameters, the resulting intensity (brightness) is more strictly correlated to absolute material density and can thus be compared across samples. In Figure 7a we see that the PU fibers contain a high-intensity lining on the external surface of each fiber, indicating that a higher density PEDOT coating was formed around each lower density PU fiber. To confirm this interpretation, we performed EDS analysis on this same fiber as indicated in Figure 7b (note some beam damage after prolonged electron beam exposure) and mapped the Mo and S

composition using Energy Dispersive X-ray Spectroscopy (EDS). Here we show both Mo and S together because these elements are unique to the PEDOT coating. We note that oMLD PEDOT films grown using EDOT and MoCl₅ are known to contain residual MoCl_x at a near stoichiometric quantity with EDOT monomers. Comparing the intensity data in Figure 7a to the EDS data in Figure 7c we observe that, indeed, the increased intensity near the edge of each PU fiber corresponds to an increased quantity of S and Mo consistent with a PEDOT layer. This SEM/EDS data confirms that the EDOT and MoCl₅ precursors are reaching the fibers within the center of each 1" sponge piece and reacting to form a conformal PEDOT layer on these fibers.

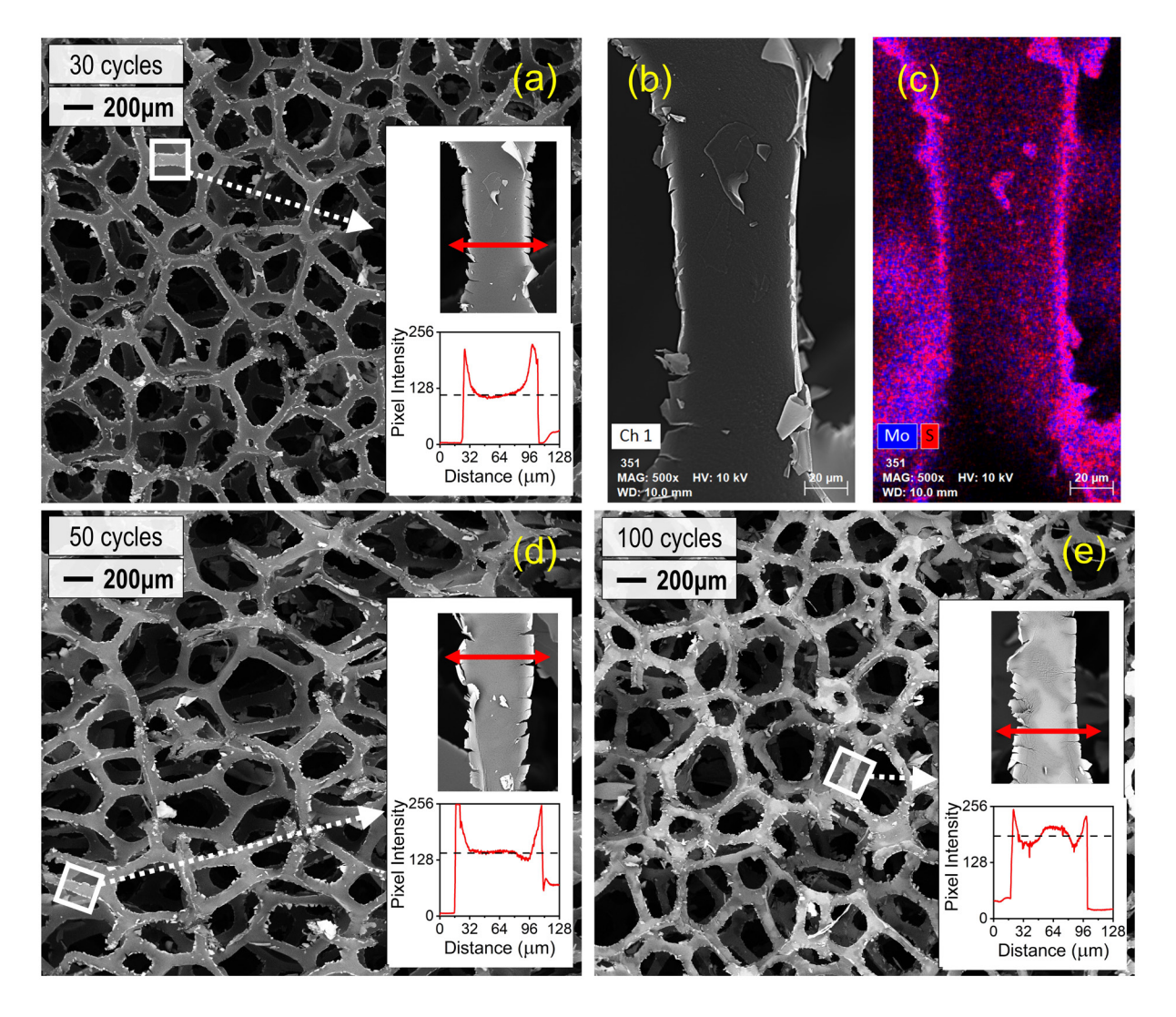


Figure 7. Scanning electron microscopy (SEM) characterization at the center of 1" PU foam cubes after 30 (a-c), 50 (d), and 100 (e) oMLD cycles of EDOT/MoCl5. All the samples here have been coated under the optimized growth conditions of a 20 s EDOT dose, 20 s EDOT purge, 500 s MoCl5 dose, and 20 s MoCl5 purge. Panels (a), (d), and (e) demonstrate (via backscatter imaging) the extent of the coating over a 3.66 mm field, with the insets characterizing the coating on individual fibers as a function of pixel intensity across the face. EDS hypermapping (b-c) confirms the high-intensity regions to be correlated with Mo and S, consistent with EDOT/MoCl5 precursors.

To confirm that the decrease in resistance with increasing number of oMLD cycles shown in Figure 6 corresponds to an increase in the thickness/loading of PEDOT, we compare the BSD SEM micrographs after 30 oMLD cycles (Figure 7a), 50 oMLD cycles (Figure 7d) and 100 oMLD cycles (Figure 7e). Qualitatively we observe an increase in the average intensity of each SEM image with an increasing number of oMLD cycles, consistent with an increase in PEDOT thickness/loading.

We note that the thickness of PEDOT on Si wafers placed adjacent to each PU sponge analyzed in Figure 7 were measured to be 32 nm, 88 nm, and 120 nm for 30, 50, and 100 oMLD cycles, respectively. We also measured the mass change of the PU sponges after oMLD growth. The initial mass of uncoated sponges was 363 ± 6 mg, and the mass of the sponges depicted in Figure 7 after oMLD growth were 270 mg, 320 mg, and 367 mg, following 30, 50, and 100 oMLD cycles, respectively. These final masses correspond to -25% -12%, and +1% changes in mass, respectively, relative to the initial PU foam mass. We attribute the net decrease or neutral mass change to the chemical decomposition and release of volatile byproducts from the PU fibers during MoCl₅ exposure, as described above surrounding Figure 3. We note that the decomposition and removal of mass from PU by MoCl₅ exposure is reminiscent of molecular layer etching⁶⁷ and atom layer etching processes⁶⁸ reported in recent years, but the initial indications in this work do not suggest that this etching process is self-limiting for MoCl₅ exposure to PU. Further insights into the deposition of oMLD PEDOT onto PU foam fibers is gained by examining higher resolution SEM images of individual PU fibers in the insets of Figure 7a, 7d, and 7e. In each of these three panels of Figure 7, we show an individual PU fiber and plot the pixel intensity along the crosssection each fiber as indicated. In general, we observe that the average intensity within each fiber increases with an increasing number of oMLD cycles as indicated by the horizontal dashed lines in each inset. This is consistent with the qualitative observation of increasing intensity with increasing number of oMLD cycles across the wide field in Figures 7a, 7d, and 7e, and supports an increased mass loading with increasing oMLD cycles. However, these SEM images also reveal additional insights into the nature of the oMLD growth process on the PU fibers. First, we observe rough/torn edges on each of the PU fibers after oMLD growth. We attribute this to the disintegration and etching of PU upon MoCl₅ exposure as described above surrounding Figure 3. We also note that there is a distinct increase in intensity with maxima at the peripheries of each fiber, to a depth of up to ~8 um. This dimension is ~100 times larger than the thickness of 50 nm measured on Si wafers adjacent to the PU sponge and suggests that the MoCl₅ and EDOT precursors are infiltrating into the bulk PU fibers, providing both a primary external PEDOT coating and secondary PEDOT layer infiltrated into the PU fibers. This behavior is consistent with prior observations for the infiltration of organometallic precursors into bulk polymers. 43-46,66

These combined processes of (1) PU etching by MoCl₅ and (2) vapor phase infiltration of EDOT and MoCl₅ into the PU fibers are expected to give rise to nonlinear changes in mechanical

properties vs. the number of PEDOT oMLD cycles. In Figure 8a we report the σ vs. ε curves during mechanical compression and decompression for PU sponges coated with 10, 30, 50, and 100 oMLD cycles. In Figure 8b we report the average σ_{avg} measured over $0.1 \le \epsilon \le 0.4$ for each of these sponges. The value of σ_{avg} increase from 0.96 psi for uncoated PU up to 2.1 \pm 0.1 psi measured for 30 oMLD cycles, and then decreases to 1.9 ± 0.1 psi at 50 oMLD cycles and $1.6 \pm$ 0.4 psi at 100 oMLD cycles in Figure 7b. Likewise, in Figure 8c we plot E on decompression for each of the sponges depicted in Figure 8a. The value of E increases with an increasing number of oMLD cycles up to a value of 49.2 psi for 50 oMLD cycles and then increase by only 8% up to a value of 53.0 psi after 100 oMLD cycles. These trends in σ_{avg} and E are consistent with our expectations based on the combined effects of (1) the infiltration and incorporation of more PEDOT with a higher number of oMLD cycles and (2) the reaction of MoCl₅ with the PU fibers as outlined in Figure 3. Rigid, dense PU has a Young's modulus ~500 psi, ⁶⁹ whereas PEDOT has a Young's modulus of ~200,000 psi. 70 This ~400-fold higher Young's modulus of PEDOT relative to PU means that a greater mass fraction of PEDOT within a PU sponge will give rise to higher values of σ_{avg} and E. However, under extended MoCl₅ exposure, more PU will be etched away, leading to a decrease in σ_{avg} and E. We attribute the increase and levelling off that we observe for σ_{avg} and E vs. the number of oMLD PEDOT cycles in Figure 8 to the superposition of these effects.

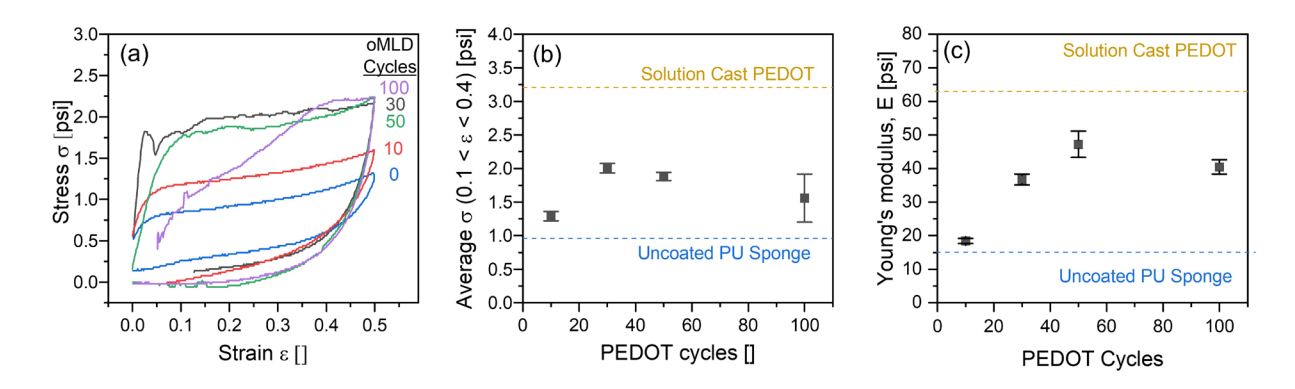


Figure 8. Effect of the number of oMLD growth cycles on the mechanical properties of PEDOT-coated PU formed using 30 oMLD cycles with a 20 s EDOT dose, 20 s EDOT purge, 500 s MoCl₅ dose, and 20 s MoCl₅ purge, including (a) stress vs. strain during compression at a strain rate of 0.1 in/min, (b) σ_{avg} on compression measured over $0.1 \le \epsilon \le 0.4$ from (a) vs. number of oMLD cycles, and (c) Young's modulus on decompression from (a) vs. number of oMLD cycles.

Stability of PEDOT-coated PU sponges

To be useful in electrochemical devices, these sponge electrodes must effectively balance (1) high electrical conductivity, (2) low compressive stress for pore collapse, and (3) low Young's modulus for more elastic recovery of foam pores. Based on the composite data collected above, we identified that, of the conditions explored in this work, 50 oMLD PEDOT cycles grown using a 20 s EDOT purge time provide the best balance of electrical conductivity and mechanical compressibility. However, to be useful as porous compressible electrodes, these PU foams must maintain these electrical and mechanical properties under repeated mechanical compression and exposure to electrolyte solutions. Based on this, we performed extended mechanical cycling of PU foams coated with PEDOT using these conditions and examined changes in the electrical conductivity and mechanical properties in Figure 9. Here, we control the strain (Figure 9a) using the compression tester described above and simultaneously measure the stress (Figure 9b) and electrical resistance (Figure 9c) during extended mechanical cycling for up to 400 mechanical compression/decompression cycles. We report the mechanical stress vs. strain data for these PEDOT-coated PU sponges as-formed (Figure 9d) and after repeated rinsing in tap water, manually wringing out the liquid, and then air-drying (Figure 9e). We also report changes in the electrical resistance as a function of mechanical compression cycles (Figure 9f) for these sponges as-formed (i), and after repeated rinsing and wringing (ii).

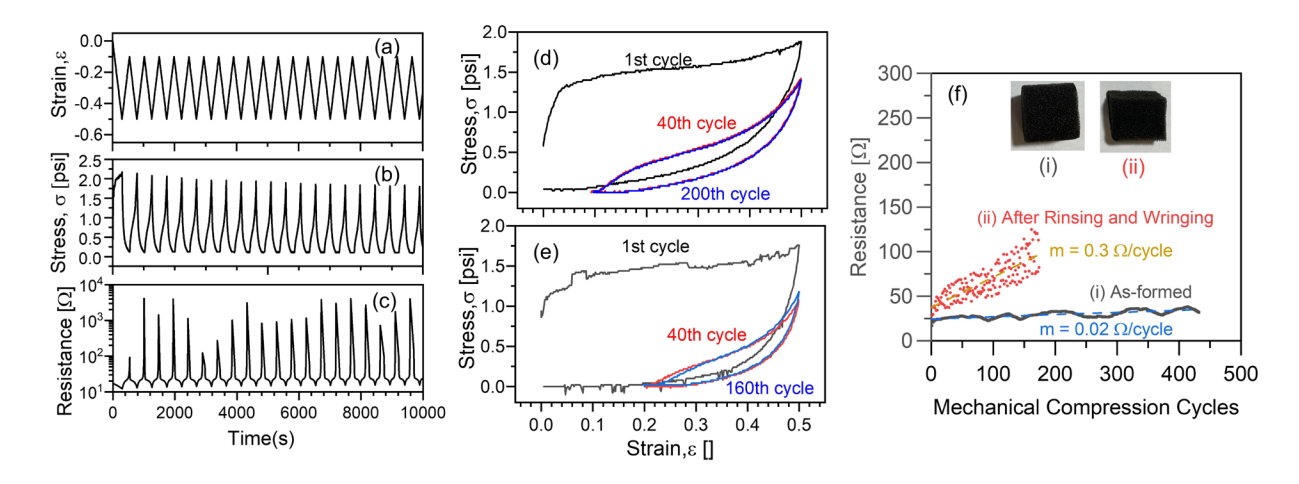


Figure 9. Stability of mechanical and electrical properties of PEDOT-coated PU sponges coated with 50 oMLD cycles using a 20 s EDOT purge time both as-formed and after repeated compression cycling and repeated rinsing in water and manual wringing, including (a) strain, (b) stress, (c) electrical resistance during first 20 mechanical compression cycles, and (d) σ vs. ε curves for 1st, 40th, and 200th compression/decompression cycle for as-formed PEDOT-coated PU sponge and (e) σ vs. ε curves for 1st, 40th, and 160th compression/decompression cycle for PEDOT-coated PU sponge after repeated rinsing in tap water and manual wringing; as well as (f) minimum values of electrical resistance for each mechanical cycle for (i) as-formed PEDOT-coated PU and (ii) after rinsing in tap water and manual wringing. The dashed lines and labeled values of slope, m, in (f) correspond to linear fits of electrical resistance vs. compression cycle.

Panels a-c of Figure 9 are exemplary data for an as-formed PEDOT coated PU sponge loaded with 50 oMLD cycles of PEDOT using the optimal growth conditions identified above. In Figure 9b and 9c, we observe that the stress and strain undergo dynamic changes during the first 20 mechanical compression cycles. In Figure 9d, process the data from Figure 9a and 9b and plot the σ vs. ε curves for select cycles, with similar data shown for a PEDOT-coated PU sponge after rinsing and wringing in Figure 9e. We observe that the mechanical response reaches steady state after 40 compression cycles, with minimal difference between the σ vs. ε curves after 40 and 200 compression cycles for the as-formed PEDOT-coated PU, and minimal differences between the σ vs. ε curves after 40 and 160 compression cycles for the PEDOT-coated PU after repeated rinsing in tap water and manual wringing. We note that this repeated mechanical cycling was performed in such a way that the strain was reduced on decompression until zero force was measured, at which point compression was reinitiated, starting the next compression cycle. Because of this, the

minimum strain on decompression reached a steady state value of ~0.1 for the as-formed PEDOT-coated PU (Figure 9d), and a value of ~0.2 for the PEDOT-coated PU after rinsing/wringing (Figure 9e). As above, these data were collected at a strain rate of 0.1 in/min. This steady state mechanical compression data in Figures 9d and 9e is analyzed in more detail below, but the convergence to repeatable steady-state mechanical compression behavior after >100 cycles generally suggests that repeated mechanical cycling does not lead to significant degradation of the mechanical properties of these sponges.

Although the PEDOT-coated PU sponges both as-formed and after rinsing/wringing reach steady state behavior, the mechanical properties we observe vary between the two. For the as-formed PEDOT-coated PU sponge, the Young's modulus on decompression during the first cycle was 29.1 psi, and decreased to 22.5 psi after 40 compression cycles and 22.1 psi after 200 compression cycles. For comparison, after repeated rinsing and mechanical wringing the Young's modulus on decompression during the first cycle was 41.0 psi, and decreased to 18.8 psi after 40 compression cycles and 17.0 psi after 160 compression cycles. Similarly, the average energy required to compress the as-formed PEDOT-coated PU foam from a strain of 0.2 to a strain of 0.5 was 26.9 mJ after 40 compression cycles and 26.4 mJ after 200 compression cycles. The energy recovered on decompression was 13.2 mJ after 40 compression cycles and 13.4 mJ after 200 compression, corresponding to ~50% energy recovery at this strain rate of 0.1 in/min. For comparison, the average energy required to compress the PEDOT-coated PU foam after rinsing/wringing from a strain of 0.2 to a strain of 0.5 was 13.8 mJ after 40 compression cycles and 13.4 mJ after 160 compression cycles. The energy recovered on decompression was 6.5 mJ after 40 compression cycles and 6.7 mJ after 160 compression cycles, corresponding to ~50% energy recovery. These data indicate that the rinsing and wringing process may remove some of the PEDOT-coated PU sponge, and/or damage the integrity of the polymer network within the PU foam, leading to a smaller amount of energy required to compress the sponge.

In Figure 9f we report the minimum electrical resistance measured at ε =0.5 vs. the number of compression/decompression cycles for both the as-formed PEDOT-coated PU, and PEDOT-coated PU following rinsing and wringing. As-formed PEDOT-coated PU exhibits a low electrical resistance of 20 Ω during initial mechanical cycling, that only increases by 0.02 Ω per compression/decompression cycle on average over >400 mechanical compression cycles. After rinsing and wringing, the PEDOT-coated PU exhibits a higher electrical resistance of 30 Ω during

initial mechanical cycling, which increases by 0.3 Ω per compression/decompression cycle on average over >150 mechanical compression cycles. Both of these sponges exhibit mean electrical resistances of $\leq 100~\Omega$ or less during the extent of mechanical testing shown in Figure 9. The higher electrical resistance observed following rinsing and ringing may arise from either (a) changes in ionic dopant concentration and state of charge or (b) mechanical degradation of the PEDOT sponge network following exposure to the manual rinsing and wringing procedure. These results are qualitative demonstrations that high electrical conductivity can be maintained even after exposure to electrochemically relevant conditions.

V. Conclusions:

This work demonstrates the formation of electrically conductive and mechanically compressible porous sponge electrodes through oxidative molecular layer deposition of PEDOT onto PU sponge supports. We identified that PU undergoes oxidative decomposition and degrades on exposure to MoCl₅, leading to mechanical embrittlement. To overcome this challenge and deliver PEDOT coatings onto PU sponges, we took advantage of vapor infiltration processes of the chemical precursors into the PU sponge fibers and reduced the purge times following the EDOT precursor dose such that MoCl₅ reacted with excess EDOT contained in/on the PU rather than with the PU itself. Using this approach, we demonstrated the ability to achieve a contiguous network of PEDOT throughout the bulk of 1" cube PU sponges. We measure electrical resistances as low as 20 Ω across the 1" foam cube while maintaining Young's Modulus and average stress on foam collapse of only 2-3 times higher than pure PU. We measured electrical resistance of $\leq 100 \Omega$ from end-toend on the sponge after manual rinsing and ringing and >150 compression/decompression cycles. The use of oMLD to deposit PEDOT provides four orders of magnitude higher electrical conductivity and a 2-3 times lower Young's Modulus as compared with solution casting. We attribute these improvements to (a) the formation of a conformal, uniform, and contiguous network of PEDOT with control over PEDOT thickness achievable by oMLD and (b) higher electrical conductivity of vapor-deposited PEDOT over solution-cast PEDOT films. This synthesis approach provides a platform for the generation of compressible, conductive electrodes with independent control over foam microstructure and redox-active material thickness. This platform can be used in future work to overcome diffusion limitations during electrochemical processes.

VI. Acknowledgements:

M.M., G.L., K.G.B., Q.K.W. and M.J.Y. acknowledge support from the National Science Foundation, Division of Chemical, Bioengineering, Environmental, and Transport Systems through award number 2131282. We thank Brian Porter at the Missouri University of Science and Technology for assistance with XPS measurements. We thank Rod Schlotzhauer, Christopher Strehl, and Ghassan Al Bahhash at the University of Missouri for assistance with fabrication of the electrical impedance test cells, and Joseph Mathai at the University of Missouri for assistance with Raman spectroscopy. We also thank Prof. Pat Kinlen, Prof. Reginald Rogers, and Prof. Matthew Maschmann at the University of Missouri for useful discussions.

VII. References:

- (1) Shi, H. Activated Carbons and Double Layer Capacitance. *Electrochim Acta* **1996**, *41*, 1633–1639. https://doi.org/10.1016/0013-4686(95)00416-5.
- Qu, D.; Shi, H. Studies of Activated Carbons Used in Double-Layer Capacitors. *J Power Sources* **1998**, 74, 99–107. https://doi.org/10.1016/S0378-7753(98)00038-X.
- (3) Frackowiak, E. Carbon Materials for the Electrochemical Storage of Energy in Capacitors. *Carbon N Y* **2001**, *39*, 937–950. https://doi.org/10.1016/S0008-6223(00)00183-4.
- (4) Wadley, H. N. G. Cellular Metals Manufacturing. *Adv Eng Mater* **2002**, *4*, 726–733. https://doi.org/10.1002/1527-2648(20021014)4:10<726::AID-ADEM726>3.0.CO;2-Y.
- (5) Banhart, J. Manufacture, Characterisation and Application of Cellular Metals and Metal Foams. *Prog Mater Sci* **2001**, *46*, 559–632. https://doi.org/10.1016/S0079-6425(00)00002-5.
- (6) Simon, P.; Gogotsi, Y. Materials for Electrochemical Capacitors. *Nat Mater* **2008**, *7*, 845–854. https://doi.org/10.1038/nmat2297.
- (7) Inagaki, M.; Konno, H.; Tanaike, O. Carbon Materials for Electrochemical Capacitors. *J Power Sources* **2010**, *195*, 7880–7903. https://doi.org/10.1016/j.jpowsour.2010.06.036.
- (8) Zhao, R.; Porada, S.; Biesheuvel, P. M.; Wal, A. Van Der; Van der Wal, A. Energy Consumption in Membrane Capacitive Deionization for Different Water Recoveries and Flow Rates, and Comparison with Reverse Osmosis. *Desalination* **2013**, *330*, 35–41. https://doi.org/10.1016/j.desal.2013.08.017.
- (9) Biesheuvel, P. M.; Zhao, R.; Porada, S.; van der Wal, a. Theory of Membrane Capacitive Deionization Including the Effect of the Electrode Pore Space. *J Colloid Interface Sci* **2011**, *360*, 239–248. https://doi.org/10.1016/j.jcis.2011.04.049.

- (10) Porada, S.; Bryjak, M.; van der Wal, A.; Biesheuvel, P. M. Effect of Electrode Thickness Variation on Operation of Capacitive Deionization. *Electrochim Acta* **2012**, *75*, 148–156. https://doi.org/10.1016/j.electacta.2012.04.083.
- (11) Lu, X.; Bertei, A.; Finegan, D. P.; Tan, C.; Daemi, S. R.; Weaving, J. S.; O'Regan, K. B.; Heenan, T. M. M.; Hinds, G.; Kendrick, E.; Brett, D. J. L.; Shearing, P. R. 3D Microstructure Design of Lithium-Ion Battery Electrodes Assisted by X-Ray Nano-Computed Tomography and Modelling. *Nat Commun* 2020, 11, 1–13. https://doi.org/10.1038/s41467-020-15811-x.
- (12) Pietsch, P.; Wood, V. X-Ray Tomography for Lithium Ion Battery Research: A Practical Guide. *Annu Rev Mater Res* **2017**, *47*, 451–479. https://doi.org/10.1146/annurev-matsci-070616-123957.
- (13) Pasta, M.; Wessells, C. D.; Cui, Y.; Mantia, F. La; La Mantia, F.; Mantia, F. La. A Desalination Battery. *Nano Lett* **2012**, *12*, 839–843. https://doi.org/10.1021/nl203889e.
- (14) Lee, J.; Kim, S.; Yoon, J. Rocking Chair Desalination Battery Based on Prussian Blue Electrodes. *ACS Omega* **2017**, *2*, 1653–1659. https://doi.org/10.1021/acsomega.6b00526.
- (15) Pothanamkandathil, V.; Fortunato, J.; Gorski, C. A. Electrochemical Desalination Using Intercalating Electrode Materials: A Comparison of Energy Demands. *Environ Sci Technol* **2020**, *54*, 3653–3662. https://doi.org/10.1021/acs.est.9b07311.
- (16) Zhao, P.; Zhang, H.; Zhou, H.; Yi, B. Nickel Foam and Carbon Felt Applications for Sodium Polysulfide/Bromine Redox Flow Battery Electrodes. *Electrochim Acta* **2005**, *51*, 1091–1098. https://doi.org/10.1016/j.electacta.2005.06.008.
- (17) Chinthaginjala, J. K.; Seshan, K.; Lefferts, L. Preparation and Application of Carbon-Nanofiber Based Microstructured Materials as Catalyst Supports. *Ind Eng Chem Res* **2007**, *46*, 3968–3978. https://doi.org/10.1021/ie061394r.
- (18) Bidault, F.; Brett, D. J. L.; Middleton, P. H.; Abson, N.; Brandon, N. P. A New Application for Nickel Foam in Alkaline Fuel Cells. *Int J Hydrogen Energy* **2009**, *34*, 6799–6808. https://doi.org/10.1016/j.ijhydene.2009.06.035.
- (19) Zheng, W.; Liu, M.; Lee, L. Y. S. Best Practices in Using Foam-Type Electrodes for Electrocatalytic Performance Benchmark. *ACS Energy Lett* **2020**, *5*, 3260–3264. https://doi.org/10.1021/acsenergylett.0c01958.
- (20) Jaugstetter, M.; Blanc, N.; Kratz, M.; Tschulik, K. Electrochemistry under Confinement. *Chem Soc Rev* **2022**, *51*, 2491–2543. https://doi.org/10.1039/d1cs00789k.
- (21) Seo, M.; Chung, T. D. Nanoconfinement Effects in Electrochemical Reactions. *Curr Opin Electrochem* **2019**, *13*, 47–54. https://doi.org/10.1016/j.coelec.2018.10.011.
- (22) Edwards, M. A.; Robinson, D. A.; Ren, H.; Cheyne, C. G.; Tan, C. S.; White, H. S. Nanoscale Electrochemical Kinetics & Dynamics: The Challenges and Opportunities of

- Single-Entity Measurements. *Faraday Discuss* **2018**, *210*, 9–28. https://doi.org/10.1039/c8fd00134k.
- (23) Kim, J. H.; Kang, T. J. Diffusion and Current Generation in Porous Electrodes for Thermo-Electrochemical Cells. *ACS Appl Mater Interfaces* **2019**, *11*, 28894–28899. https://doi.org/10.1021/acsami.9b08381.
- (24) Wan, C. T.-C.; Greco, K. V.; Alazmi, A.; Darling, R. M.; Chiang, Y.-M.; Brushett, F. R. Methods—A Potential—Dependent Thiele Modulus to Quantify the Effectiveness of Porous Electrocatalysts. *J Electrochem Soc* **2021**, *168*, 123503. https://doi.org/10.1149/1945-7111/ac34ce.
- (25) Kang, N.; Lin, Y.; Yang, L.; Lu, D.; Xiao, J.; Qi, Y.; Cai, M. Cathode Porosity Is a Missing Key Parameter to Optimize Lithium-Sulfur Battery Energy Density. *Nat Commun* **2019**, *10*, 1–10. https://doi.org/10.1038/s41467-019-12542-6.
- (26) Song, J.; Kim, J.; Kang, T.; Kim, D. Design of a Porous Cathode for Ultrahigh Performance of a Li-Ion Battery: An Overlooked Pore Distribution. *Sci Rep* **2017**, *7*, 1–8. https://doi.org/10.1038/srep42521.
- (27) Liu, H.; Wu, S.; Tian, N.; Yan, F.; You, C.; Yang, Y. Carbon Foams: 3D Porous Carbon Materials Holding Immense Potential. *J Mater Chem A Mater* **2020**, *8*, 23699–23723. https://doi.org/10.1039/d0ta08749a.
- (28) Prehal, C.; Weingarth, D.; Perre, E.; Lechner, R. T.; Amenitsch, H.; Paris, O.; Presser, V. Tracking the Structural Arrangement of Ions in Carbon Supercapacitor Nanopores Using in Situ Small-Angle X-Ray Scattering. *Energy Environ Sci* **2015**, *8*, 1725–1735. https://doi.org/10.1039/c5ee00488h.
- (29) Sun, H.; Xu, Z.; Gao, C. Multifunctional, Ultra-Flyweight, Synergistically Assembled Carbon Aerogels. *Advanced Materials* **2013**, *25*, 2554–2560. https://doi.org/10.1002/adma.201204576.
- (30) Zhang, X.; Sui, Z.; Xu, B.; Yue, S.; Luo, Y.; Zhan, W.; Liu, B. Mechanically Strong and Highly Conductive Graphene Aerogel and Its Use as Electrodes for Electrochemical Power Sources. *J Mater Chem* **2011**, *21*, 6494–6497. https://doi.org/10.1039/c1jm10239g.
- (31) Gui, X.; Wei, J.; Wang, K.; Cao, A.; Zhu, H.; Jia, Y.; Shu, Q.; Wu, D. Carbon Nanotube Sponges. *Advanced Materials* **2010**, *22*, 617–621. https://doi.org/10.1002/adma.200902986.
- (32) Zhang, F.; Feng, Y.; Qin, M.; Gao, L.; Li, Z.; Zhao, F.; Zhang, Z.; Lv, F.; Feng, W. Stress Controllability in Thermal and Electrical Conductivity of 3D Elastic Graphene-Crosslinked Carbon Nanotube Sponge/Polyimide Nanocomposite. *Adv Funct Mater* **2019**, 29. https://doi.org/10.1002/adfm.201901383.

- (33) Yuan, S.; Fan, W.; Wang, D.; Zhang, L.; Miao, Y. E.; Lai, F.; Liu, T. 3D Printed Carbon Aerogel Microlattices for Customizable Supercapacitors with High Areal Capacitance. *J Mater Chem A Mater* **2021**, *9*, 423–432. https://doi.org/10.1039/d0ta08750e.
- (34) Zhao, Y.; Liu, J.; Hu, Y.; Cheng, H.; Hu, C.; Jiang, C.; Jiang, L.; Cao, A.; Qu, L. Highly Compression-Tolerant Supercapacitor Based on Polypyrrole-Mediated Graphene Foam Electrodes. *Advanced Materials* **2013**, *25*, 591–595. https://doi.org/10.1002/adma.201203578.
- (35) Liang, X.; Nie, K.; Ding, X.; Dang, L.; Sun, J.; Shi, F.; Xu, H.; Jiang, R.; He, X.; Liu, Z.; Lei, Z. Highly Compressible Carbon Sponge Supercapacitor Electrode with Enhanced Performance by Growing Nickel-Cobalt Sulfide Nanosheets. *ACS Appl Mater Interfaces* **2018**, *10*, 10087–10095. https://doi.org/10.1021/acsami.7b19043.
- (36) Yang, Y.; Tu, Y.; Zhu, P.; Zhang, L.; Li, T.; Zheng, H.; Sun, R.; Wong, C. A Cobalt Hydroxide-Based Compressible Electrode Material for Asymmetrical All-Solid Supercapacitors. *Sustain Energy Fuels* **2018**, *2*, 2345–2357. https://doi.org/10.1039/c8se00409a.
- (37) Wang, Y.; Sotzing, G. A.; Weiss, R. A. Preparation of Conductive Polypyrrole/Polyurethane Composite Foams by in Situ Polymerization of Pyrrole. *Chemistry of Materials* **2008**, *20*, 2574–2582. https://doi.org/10.1021/cm800005r.
- (38) Mano, G.; Murasawa, Y.; Shimamura, K.; Iso, A.; Kanehashi, S.; Shimomura, T. Fabrication, Characterization, and Thermoelectric Properties of Soft Polyurethane Foam Loaded with Semiconducting Poly(3-Hexylthiophene) Nanofibers. *J Appl Polym Sci* **2022**, *139*, 1–8. https://doi.org/10.1002/app.52354.
- (39) Liu, Y.; Li, W.; Kick, C.; Zhao, X.; Wu, H. Preparation of Polypyrrole/Polyurethane Foam Composite Material. *Fibres and Textiles in Eastern Europe* **2020**, *28*, 69–73. https://doi.org/10.5604/01.3001.0013.9022.
- (40) He, F.; Omoto, M.; Yamamoto, T.; Kise, H. Preparation of Polypyrrole–Polyurethane Composite Foam by Vapor Phase Oxidative Polymerization. *J Appl Polym Sci* **1995**, *55*, 283–287. https://doi.org/10.1002/app.1995.070550211.
- (41) Bessette, M. D.; Weiss, R. A.; Gan, P. P.; Erkey, C.; Fu, Y. Conductive Elastomeric Foams By In-Situ Vapor Phase Polymerization Of Pyrroles. 6156235, 2000.
- (42) Moehwald, H. Composite Material Consisting Of Porous Materials And Electrically Conductive Polymers. 4636430, 1987.
- (43) Eldridge, J. J.; Crockett, R. M.; Maund, J. R.; Leonard, D.; Mcnaught, R. H.; Li, W.; Filippenko, a V; Lupton, R. H.; Frogel, J. a; Humphreys, R. M.; et al. Greatly Increased Toughness of Infiltrated Spider Silk. *Science* (1979) **2012**, 324, 488–492.

- (44) Peng, Q.; Tseng, Y. C.; Darling, S. B.; Elam, J. W. Nanoscopic Patterned Materials with Tunable Dimensions via Atomic Layer Deposition on Block Copolymers. *Advanced Materials* **2010**, *22*, 5129–5133. https://doi.org/10.1002/adma.201002465.
- (45) Gong, B.; Peng, Q.; Jur, J. S.; Devine, C. K.; Lee, K.; Parsons, G. N. Sequential Vapor Infiltration of Metal Oxides into Sacrificial Polyester Fibers: Shape Replication and Controlled Porosity of Microporous/Mesoporous Oxide Monoliths. *Chemistry of Materials* **2011**, *23*, 3476–3485. https://doi.org/10.1021/cm200694w.
- (46) Leng, C. Z.; Losego, M. D. Vapor Phase Infiltration (VPI) for Transforming Polymers into Organic-Inorganic Hybrid Materials: A Critical Review of Current Progress and Future Challenges. *Mater Horiz* **2017**, *4*, 747–771. https://doi.org/10.1039/c7mh00196g.
- (47) Atanasov, S. E.; Losego, M. D.; Gong, B.; Sachet, E.; Maria, J. P.; Williams, P. S.; Parsons, G. N. Highly Conductive and Conformal Poly(3,4-Ethylenedioxythiophene) (PEDOT) Thin Films via Oxidative Molecular Layer Deposition. *Chemistry of Materials* **2014**, *26*, 3471–3478. https://doi.org/10.1021/cm500825b.
- (48) Wyatt, Q. K.; Brathwaite, K. G.; Ardiansyah, M.; Paranamana, N. C.; Brorsen, K. R.; Young, M. J. Mechanistic Insights into Oxidative Molecular Layer Deposition of Conjugated Polymers. *Chemistry of Materials* **2023**, *35*, 154–162. https://doi.org/10.1021/acs.chemmater.2c02923.
- (49) Volk, A. A.; Kim, J.-S.; Jamir, J.; Dickey, E. C.; Parsons, G. N. Oxidative Molecular Layer Deposition of PEDOT Using Volatile Antimony(V) Chloride Oxidant. *Journal of Vacuum Science & Technology A* **2021**, *39*, 032413. https://doi.org/10.1116/6.0000791.
- (50) Brathwaite, K. G.; Wyatt, Q. K.; Atassi, A.; Gregory, S. A.; Throm, E.; Stalla, D.; Yee, S. K.; Losego, M. D.; Young, M. J. Effects of Film Thickness on Electrochemical Properties of Nanoscale Polyethylenedioxythiophene (PEDOT) Thin Films Grown by Oxidative Molecular Layer Deposition (OMLD). *Nanoscale* 2023, 14–16. https://doi.org/10.1039/D3NR00708A.
- (51) Elam, J. W.; Groner, M. D.; George, S. M. Viscous Flow Reactor with Quartz Crystal Microbalance for Thin Film Growth by Atomic Layer Deposition. *Review of Scientific Instruments* **2002**, *73*, 2981–2987. https://doi.org/10.1063/1.1490410.
- (52) Paranamana, N. C.; He, X.; Young, M. J. Atomic Layer Deposition of Thin-Film Sodium Manganese Oxide Cathode Materials for Sodium Ion Batteries. *Dalton Transactions* **2021**, 50, 18128–18142. https://doi.org/10.1039/d1dt03479k.
- (53) Wyatt, Q. K.; Vaninger, M.; Paranamana, N. C.; Heitmann, T. W.; Kaiser, H.; Young, M. J. Oxidative Molecular Layer Deposition of Amine-Containing Conjugated Polymer Thin Films. *ACS Appl Polym Mater* **2022**. https://doi.org/10.1021/acsapm.2c00942.
- (54) Bednarski, H.; Hajduk, B.; Jurusik, J.; Jarzabek, B.; Domanski, M.; Łaba, K.; Wanic, A.; Łapkowski, M. The Influence of PEDOT to PSS Ratio on the Optical Properties of

- PEDOT: PSS Thin Solid Films Insight from Spectroscopic Ellipsometry. *Acta Phys Pol A* **2016**, *130*, 1242–1244. https://doi.org/10.12693/APhysPolA.130.1242.
- (55) Hwang, J.; Tanner, D. B.; Schwendeman, I.; Reynolds, J. R. Optical Properties of Nondegenerate Ground-State Polymers: Three Dioxythiophene-Based Conjugated Polymers. *Phys Rev B Condens Matter Mater Phys* 2003, 67, 10. https://doi.org/10.1103/PhysRevB.67.115205.
- (56) Hwang, J.; Schwendeman, I.; Ihas, B. C.; Clark, R. J.; Cornick, M.; Nikolou, M.; Argun, A.; Reynolds, J. R.; Tanner, D. B. In Situ Measurements of the Optical Absorption of Dioxythiophene-Based Conjugated Polymers. *Phys Rev B Condens Matter Mater Phys* 2011, 83, 1–12. https://doi.org/10.1103/PhysRevB.83.195121.
- (57) Nie, S.; Li, Z.; Yao, Y.; Jin, Y. Progress in Synthesis of Conductive Polymer Poly(3,4-Ethylenedioxythiophene). *Front Chem* **2021**, *9*, 1–8. https://doi.org/10.3389/fchem.2021.803509.
- (58) Włodarczak, D. Studies of Temperature and Atmosphere Composition Influence on Thermal Degradation Products of Polyurethane Foam. *J Appl Polym Sci* **1988**, *36*, 377–386. https://doi.org/10.1002/app.1988.070360210.
- (59) Jellinek, H. H. G.; Dunkle, S. R. Kinetics and Mechanism of Hcn-Evolution From the Oxidation of Polyurethanes. *J Polym Sci A1* **1983**, *21*, 487–511. https://doi.org/10.1002/pol.1983.170210218.
- (60) Bolland, J. L.; Gee, G. Kinetic Studies in the Chemistry of Rubber and Related Materials. II. The Kinetics of Oxidation of Unconjugated Olefins. *Transactions of the Faraday Society*. 1946, pp 236–243. https://doi.org/10.1039/TF9464200236.
- (61) Khatua, S.; Hsieh, Y. Lo. Chlorine Degradation of Polyether-Based Polyurethane. *J Polym Sci A Polym Chem* **1997**, *35*, 3263–3273. https://doi.org/10.1002/(SICI)1099-0518(19971115)35:15<3263::AID-POLA20>3.0.CO;2-8.
- (62) Bruckmoser, K.; Resch, K. Investigation of Ageing Mechanisms in Thermoplastic Polyurethanes by Means of IR and Raman Spectroscopy. *Macromol Symp* **2014**, *339*, 70–83. https://doi.org/10.1002/masy.201300140.
- (63) Parnell, S.; Min, K.; Cakmak, M. Kinetic Studies of Polyurethane Polymerization with Raman Spectroscopy. *Polymer (Guildf)* **2003**, *44*, 5137–5144. https://doi.org/10.1016/S0032-3861(03)00468-3.
- (64) Xu, L.; Li, C.; Ng, K. Y. S. In-Situ Monitoring of Urethane Formation by FTIR and Raman Spectroscopy. *Journal of Physical Chemistry A* **2000**, *104*, 3952–3957. https://doi.org/10.1021/jp992622g.
- (65) Jain, H.; Poodt, P. About the Importance of Purge Time in Molecular Layer Deposition of Alucone Films. *Dalton Transactions* **2021**, *50*, 5807–5818. https://doi.org/10.1039/d1dt00623a.

- (66) Ren, Y.; McGuinness, E. K.; Huang, C.; Joseph, V. R.; Lively, R. P.; Losego, M. D. Reaction-Diffusion Transport Model to Predict Precursor Uptake and Spatial Distribution in Vapor-Phase Infiltration Processes. *Chemistry of Materials* **2021**, *33*, 5210–5222. https://doi.org/10.1021/acs.chemmater.1c01283.
- (67) Young, M. J.; Choudhury, D.; Letourneau, S.; Mane, A.; Yanguas-Gil, A.; Elam, J. W. Molecular Layer Etching of Metalcone Films Using Lithium Organic Salts and Trimethylaluminum. *Chemistry of Materials* 2020, 32, 992–1001. https://doi.org/10.1021/acs.chemmater.9b03627.
- (68) George, S. M.; Lee, Y. Prospects for Thermal Atomic Layer Etching Using Sequential, Self-Limiting Fluorination and Ligand-Exchange Reactions. *ACS Nano* **2016**, *10*, 4889–4894. https://doi.org/10.1021/acsnano.6b02991.
- (69) Rampf, M.; Speck, O.; Speck, T.; Luchsinger, R. H. Structural and Mechanical Properties of Flexible Polyurethane Foams Cured under Pressure. *Journal of Cellular Plastics* **2012**, 48, 53–69. https://doi.org/10.1177/0021955X11429171.
- (70) Lang, U.; Naujoks, N.; Dual, J. Mechanical Characterization of PEDOT:PSS Thin Films. *Synth Met* **2009**, *159*, 473–479. https://doi.org/10.1016/j.synthmet.2008.11.005.